doi.org/10.26434/chemrxiv.9764924.v1

Synthesis of a Structurally Perfect d1 Kagome Lattice Antiferromagnet, (CH3NH3)2NaTi3F12

Ningxin Jiang, Arun Ramanathan, John Bacsa, Henry La Pierre

Submitted date: 03/09/2019 • Posted date: 06/09/2019

Citation information: Jiang, Ningxin; Ramanathan, Arun; Bacsa, John; La Pierre, Henry (2019): Synthesis of a Structurally Perfect d1 Kagome Lattice Antiferromagnet, (CH3NH3)2NaTi3F12. ChemRxiv. Preprint.

S = 1 /2 kagome lattice antiferromagnets (KLAFs) have attracted great interest since they are closely associated with the long-sought quantum spin liquid (QSL) state. The realization of S = 1/2 KLAF remains an outstanding challenge and efforts have focused principally on Cu2+, d9 compounds. Herein, the synthesis of the first structurally perfect d1 KLAF, (CH3NH3)2NaTi3F12, is presented. The trivalent oxidation state and the Jahn-Teller distortion of Ti3+ ions are probed by single crystal X-ray diffraction, X- ray photoelectron spectroscopy, and UV-vis-NIR diffuse reflectance. No structural phase transitions can be observed from 1.8 K to 523 K. However, a glass transition can be observed due to the disordered, interlayer CH3NH3+ cations. The Curie-Weiss temperature, θcw= -139.5(7) K, and the lack of long-range ordering in magnetic susceptibility and specific heat imply that this compound is a QSL candidate.

File list (2)

Synthesis of a Structurally Perfect d^1 Kagome Lattice Antiferromagnet, $(CH_3NH_3)_2NaTi_3F_{12}$

Ningxin Jiang[1], Arun Ramanathan[1], John Bacsa[1], and Henry S. La Pierre[1,2]*

[1]School of Chemistry and Biochemistry and the [2]Nuclear and Radiological Engineering Program, School of Mechanical Engineering, Georgia Institute of Technology, Atlanta, Georgia 30332-0400, United States. *e-mail: hsl@gatech.edu

Abstract: S = 1 /2 kagome lattice antiferromagnets (KLAFs) have attracted great interest since they are closely associated with the long-sought quantum spin liquid (QSL) state. The realization of S = 1/2 KLAF remains an outstanding challenge and efforts have focused principally on Cu^{2+}, d^9 compounds. Herein, the synthesis of the first structurally perfect d^1 KLAF, $(CH_3NH_3)_2NaTi_3F_{12}$, is presented. The trivalent oxidation state and the Jahn-Teller distortion of Ti^{3+} ions are probed by single crystal X-ray diffraction, X-ray photoelectron spectroscopy, and UV-vis-NIR diffuse reflectance. No structural phase transitions can be observed from 1.8 K to 523 K. However, a glass transition can be observed due to the disordered, interlayer $CH_3NH_3^+$ cations. The Curie-Weiss temperature, θ_{cw}= -139.5(7) K, and the lack of long-range ordering in magnetic susceptibility and specific heat imply that this compound is a QSL candidate.

Geometrically frustrated magnets have been studied extensively due to their potential for engendering unusual magnetic and electronic states.[1] The kagome lattice, which is composed of a planar array of the corner-sharing triangles, is one of the most geometrically frustrated lattices.[2] Several S > 1/2 kagome lattice magnets have been synthesized,[3-6] and novel magnetic behaviors such as spin chirality are realized in these compounds due to the strong magnetic frustration.[7,8] The S = 1/2 kagome lattice antiferromagnet (KLAF) is of particular interest since it can host the long-sought quantum spin liquid (QSL) state.[9,10] However, the experimental realization of S = 1/2 KLAF is not trivial.

Syntheses of several S = 1/2 KLAFs have been developed, but none of these compounds have a perfect 2D kagome lattice. Herbertsmithite, $ZnCu_3(OH)_6Cl_2$, with perfect Cu^{2+}-based kagome lattice layers, is a prime QSL candidate compound.[11,12] Nevertheless, more than 5% of the interlayer Zn^{2+} sites between layers are occupied by Cu^{2+}, which potentially break the magnetic two-dimensionality.[13,14] Distortion of the kagome lattice is another problem that several S = 1/2 KLAFs present. In $BaCu_3V_2O_8(OH)_2$, two inequivalent Cu^{2+} sites and Cu–Cu distances are observed in each triangular unit which is proposed to lead to the transition to the spin-glass state at 9 K instead of a QSL state.[15,16] Apart from these Cu^{2+} based compounds, a rare d^1 ion based KLAF, $[NH_4]_2[C_7H_{14}N][V_7O_6F_{18}]$, has been synthesized by an ionothermal method.[17] Despite the QSL behaviors observed in this compound, the weakly-interacting V^{3+} ions between the layers and the two different V^{4+}–V^{4+} distances observed in the kagome layers lead to deviation in this compound from a perfect S = 1/2 KLAF.[18] Therefore, the synthesis of perfect S = 1/2 KLAF remains an open challenge.

Historically, S = 1/2 KLAFs are mainly based on d^9, Cu^{2+} ion. Ions with d^1 configurations, such as Ti^{3+} or V^{4+}, have attracted less attention – ostensibly due to the greater redox instability of these ions.[19] Trivalent titanium, d^1, Ti^{3+}, is potentially attractive for the design of quantum magnetic materials since it has substantially smaller spin-orbit coupling (0.0153 μm^{-1} in comparison to Cu at 0.0829 μm^{-1}).[20,21] Additionally, the Jahn-Teller distortion of the coordination octahedra is expected to be compressive in contrast to d^9 ions and presents unique design opportunities.[21] It is notable that the synthesis of several

air-stable trivalent titanium fluoride compounds have been reported which suggest that the fluoride ligand might be important for the stabilization of trivalent titanium in aqueous synthetic conditions.[22-24] This hypothesis has been further supported by a recent study on three strongly distorted KLAFs, $Rb_2NaTi_3F_{12}$, $Cs_2NaTi_3F_{12,}$ and $Cs_2KTi_3F_{12}$.[25] The experimental and theoretical studies suggest that such distorted S = 1/2 KLAFs compounds possess magnetic behaviors bridging one-dimensional and two-dimensional behaviors.[21,25] Nonetheless, this group of compounds provides a structural template, $A_2BTi_3F_{12}$, for designing Ti^{3+} based KLAFs.

Herein, a Ti^{3+} based, structurally perfect KLAF, $(CH_3NH_3)NaTi_3F_{12}$ (**1-Ti**), has been synthesized by a hydrothermal method. One distinct Ti^{3+} site is found in the kagome lattice layer, and the distances between the nearest-neighboring Ti^{3+} are all 3.8523(1) Å. The trivalent oxidation state of the titanium and the compressive Jahn-Teller distortion are demonstrated by room temperature single crystal X-ray diffraction (SCXRD), X-ray photoelectron spectroscopy (XPS) and UV-vis-NIR diffuse reflectance spectra (UV-vis-NIR DRS). The Ti^{3+}-based kagome layers are well-separated by Na^+ ions and disordered methylammonium cations, $CH_3NH_3^+$ (MA^+). The thermal behavior of **1-Ti** is studied by low-temperature SCXRD, differential scanning calorimetry (DSC), and specific heat measurements. No phase transition is observed from 1.8 to 523 K. The DSC measurement also suggest that the MA^+ exhibit a glassy behavior with decreasing temperature. The Curie-Weiss temperature, θ_{cw}= -139.5(7) K indicates a strong antiferromagnetic interaction between spins. No spin ordering is observed down to 1.8 K based on the magnetic susceptibility and specific heat measurements, which suggest that this compound is a QSL candidate. Less than 5% of magnetic impurities are observed based on the isothermal magnetization measurement.

Results and discussion

Synthesis and structural analysis. Compound **1-Ti** was prepared hydrothermally by mixing Ti powder, HPF_6 aqueous solution, NaF, and $CH_3NH_2{\cdot}HCl$ in deionized water.[26] The reaction vessel was sealed immediately after the addition of HPF_6 (gas evolution was observed immediately upon addition) and heated at 363 K for 42 hours and then cooled to room temperature at a rate of 0.5 K / minute. The use of Ti powder instead of a soluble Ti^{3+} precursor is crucial for the synthesis of **1-Ti**, since the hydrogen gas generated by the reaction between Ti^0 and HPF_6 delays the oxidation of Ti^{3+} to Ti^{4+} under the reaction conditions. In a control experiment, the reaction vessel was sealed 30 minutes after the addition of HPF_6 (and the evolved H_2 was not contained) and no trivalent titanium product was found after the reaction. The monovalent cations were carefully selected. The methylammonium cation, a widely-used multiatomic monovalent cation in organic-inorganic hybrid perovskite, was introduced to the reaction systems since the MA^+ is larger compared to the alkali metal cations and the hydrogen in MA^+ can form the strong H–F hydrogen bonds.[27,28] Control experiments with larger alkyl and aryl ammonium cations such as dimethylamine and aniline give no crystalline phases.

Pink single crystals of **1-Ti** with dimensions of ~ 0.09 mm × 0.06 mm × 0.04 mm were isolated for SCXRD at 298 K (Fig. S1). The **1-Ti** crystallizes in the trigonal space group $R\bar{3}m$. One distinct Ti^{3+} site can be found in the **1-Ti** (Fig. 1a). The Ti^{3+} ion is surrounded by four equatorial fluoride ligands with Ti–F bond length of 2.0137(4) Å and two axial fluoride ligands with Ti–F bond length of 1.8900(10) Å. The bond valence sum (BVS) calculation yielded the valence of 3.097 based on the Ti^{3+} parameters (R_{ij} = 1.723, b = 0.37 Å) but 3.422 based on the Ti^{4+} parameters (R_{ij} = 1.76, b = 0.37 Å) in **1-Ti**.[29,30] These BVS results indicate that the titanium in **1-Ti** is formally Ti^{3+}. The distortion of the octahedral environment can be assigned as a compressed Jahn-Teller distortion which leads to a local D_{4h} point group symmetry for the

Ti^{3+} with a d^1 electron configuration.[31] The fluoride ligands bridge Ti^{3+} ions to form a perfect kagomé lattice composed of $\{Ti_3F_6\}$ triangles (Fig. 1b). All the bond angles ∠Ti-F-Ti equal 146.09(4)° and distances between nearest-neighbor Ti^{3+} ions are equal to 3.8523(1) Å. Regular hexagons and equilateral triangles composed of Ti^{3+} ions can be found in the layer with all internal angles in the kagome layer are equal to either 60° or 120°. The powder X-ray diffraction (PXRD) pattern simulated from the 298 K SCXRD result matches well with the experimental PXRD pattern at 298 K (Fig. S3) which indicates the bulk purity of the product.

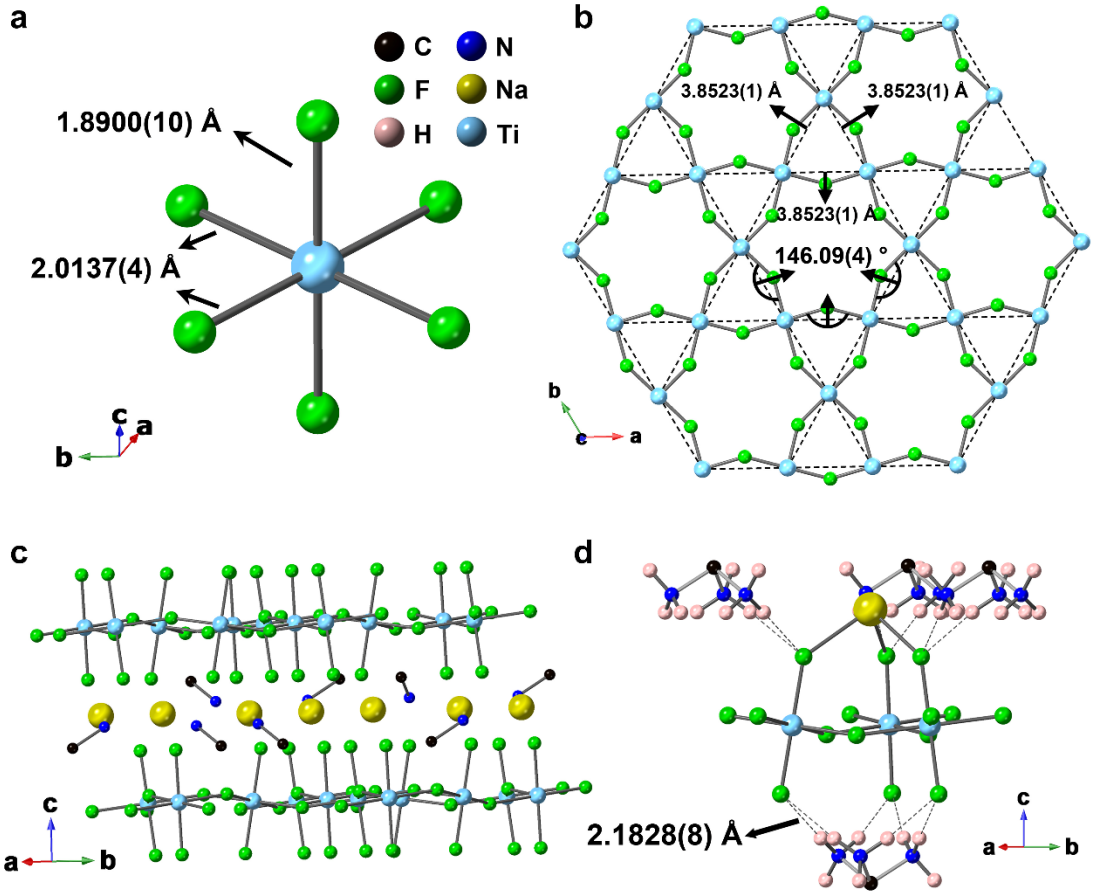

Figure 1. (a) The coordination environments of TiF_6^{3-} in **1-Ti**. (b) The $\{Ti_3F_6\}$ kagome lattice layer in **1-Ti** viewed parallel to the crystallographic *c*-axis. (c) Demonstration of the interlayer Na^+ and MA^+ in **1-Ti,** one of the three equivalent nitrogen sites is shown for each MA^+ (the position of nitrogen sites are chosen randomly to display the nitrogen positional disorder in MA^+). (d) Demonstration of the N-H···F hydrogen bond between $\{Ti_3F_6\}$ kagome lattice layer and the MA cation in **1-Ti**. All three positions of the MA cation are shown to demonstrate the disorder model. Hydrogen atoms are omitted for clarity except in (d). C1 atom sites are omitted in (c) and (d).

Sodium and methylammonium cations are located between the titanium fluoride layers (Fig. 1c). One distinct Na^+ site ligated by six fluoride ligands in perfect octahedral geometry with all the Na-F bond length of 2.3082(10) Å is found in **1-Ti.** The MA cations are disordered in **1-Ti** and can be resolved with an appropriate disordered model (Fig. S2). The positions of carbon atom in the MA^+ are reduced to two parts, C0 and C1. The C0 position with carbon occupancy of 1/2 is located right above and below the center of the titanium hexagon, which is also on the 3-fold inversion axis. The C1 position is not on the 3-fold axis or the mirror plane. Therefore, the C1 represents six symmetrically equivalent positions with each position

has a carbon occupancy of 1/12. The nitrogen atom is located on the mirror plane but not the 3-fold inversion axis. As a result, the nitrogen atoms occupy three symmetrically equivalent positions with atom occupancy of 1/3 for each site. The distance between the axial fluoride ligating to titanium and its nearest hydrogen atom from NH_3 group is 2.1828(8) Å which is within the range of the H-F hydrogen bonding distance (Fig.1d). Therefore, the orientation of the methylammonium cations in **1-Ti** could be attributed to the formation of the strong H-F hydrogen bonds between the -NH_3 groups and the fluoride ligands.[32]

Spectroscopic analysis of 1-Ti. The trivalent oxidation state of titanium in **1-Ti** derived from the charge balance and the BVS calculations was further established spectroscopically, since the oxidation state of titanium cations can vary from +2 to +4 in similar conditions.[33] The high-resolution XPS Ti 2p spectrum of **1-Ti** is shown in Fig 2a. The spectrum is resolved into three peaks. The peaks centered at 459.9 eV and 465.7 eV can be assigned as Ti $2p_{3/2}$ and Ti $2p_{1/2}$ respectively which matched well with binding energies of Ti^{3+} in TiF_3 (459.9 eV for Ti $2p_{3/2}$ and 465.5 eV for Ti $2p_{1/2}$).[34] The full width at half maximum for Ti $2p_{1/2}$ is much broader than Ti$2p_{3/2,}$ which can be attributed to the Coster-Kronig effect.[35] The peak centers at 472.1 eV can be assigned as shake-up satellites of Ti^{3+} in $(TiF_6)^{3-}$ environment.[34] Fitting the data with the inclusion of Ti^{4+} peaks (~466.9 eV for Ti $2p_{1/2}$ and ~461.6 eV for Ti $2p_{3/2}$) result in a poor fitting result which indicates that almost no Ti^{4+} can be probed on the surface of **1-Ti** compounds.[34] Since XPS probes the electronic state of elements on the surface of the sample (a few nanometers),[36] the XPS results demonstrate the predominance Ti^{3+} in the sample despite the increased potential for surface oxidation by O_2 in comparison to the bulk Ti^{3+} in the sample.

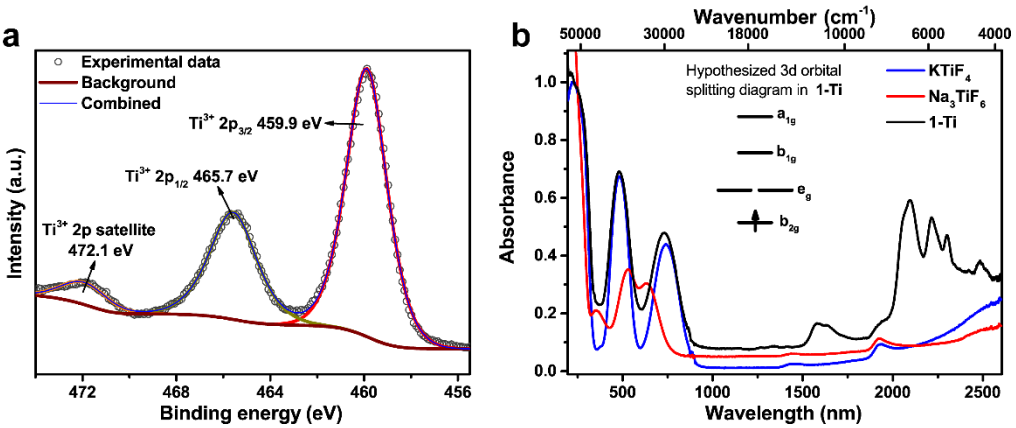

Figure 2. (a) High-resolution XPS Ti 2p spectrum of **1-Ti**. (b) UV-vis-NIR diffuse reflectance spectra of **1-Ti,** $KTiF_4$, and Na_3TiF_6. Inset: Hypothesized local 3d orbital splitting diagram in **1-Ti** based on the UV-vis-NIR data.

The UV-vis-NIR DRS range from 200 nm to 2600 nm was employed to study oxidation state and the d-orbital splitting of trivalent titanium in **1-Ti**. Ten peaks can be observed in **1-Ti** spectrum (black line in Fig. 2b). UV-vis-NIR DRS spectra of Na_3TiF_6 and $KTiF_4$ (red and blue lines in Fig. 2b) and $CH_3NH_2{\cdot}HCl$ (Fig. S9) were used as references to assign these peaks. The absorption below 400 nm can be ascribed to ligand to metal charge transfer.[31] The absorptions at 481 and 728 nm can be assigned as the d-d transitios, which are also observed in $KTiF_4$ and Na_3TiF_6. The Jahn-Teller compression causes the splitting of the t_{2g} and e_g to four different energy levels as shown in the inset of Fig. 2b and lead to two absorptions in the visible region, $^2B_{2g} \rightarrow {}^2B_{1g}$ (728 nm) and $^2B_{2g} \rightarrow {}^2A_{1g}$ (481 nm). The position of these maxima in the spectrum of **1-Ti** are closer to the maxima in the spectrum of $KTiF_4$ than those observed in the spectrum of Na_3TiF_6, since the Ti^{3+} polyhedral in $KTiF_4$ and **1-Ti** exhibit stronger Jahn-Teller compression in

comparison to Na_3TiF_6.[31] The six maxima at lower energy in **1-Ti** (1578, 1628, 2095, 2215, 2300 and 2484 nm) are similar to those observed in $CH_3NH_2{\cdot}HCl$ and can be ascribed as the characteristic absorption of the methylammonium cations.[37] A shoulder peak has been observed around 1930 nm in **1-Ti** which can be found in $CH_3NH_2{\cdot}HCl$, $KTiF_4$ and Na_3TiF_6 spectra and may be attributable to the $^2B_{2g} \rightarrow {}^2E_g$ transition.

Thermal behavior of 1-Ti. Several Cu^{2+} based KLAFs, $Cs_2MCu_3F_{12}$ (M = Zr, Hf, and Sn), which share similar crystal structure as **1-Ti** at room temperature, and a recently reported divalent titanium KLAF, $Na_2Ti_3Cl_8$ experience phase transitions from perfect kagome lattices in the $R\bar{3}m$ space group to distorted kagome lattices.[38-40] Therefore, low-temperature SCXRD, DSC, and specific heat measurement were used to exclude the existence of structural phase transition of **1-Ti**. The single crystal structure of **1-Ti** at 100 K is very close to crystal structure at 298 K. The $R\bar{3}m$ space group and the perfect kagome lattice are maintained at 100 K, and the position of each atom are nearly identical at the two temperatures, as shown in Table S1 and S2. The stability of this phase is further confirmed by variable temperature PXRD measured from 300 K to 673 K (Fig. S4), DSC measured from 183 K to 363 K (Fig. 3a) and specific heat measured from 1.8 K to 273 K (Fig 3b). The combination of no changes in PXRD patterns up to 523 K, and the absence of a sharp peak in DSC and specific heat indicate that no phase transition exists from 1.8 K to 523 K. It is noticeable that sudden changes of slope can be observed in both cooling curve and the heating curve of the DSC around 200 K and the entire phenomenon is shifted to lower temperature when the temperature scanning rates are decreased. These behaviors match well with a glass transition phenomenon, and the existence of glass transition is further supported by the observation of an anomaly in the heat capacity around 220 K (Fig 3b).[41] Therefore, we hypothesized that the nitrogen atoms in MA^+ move freely amongst the three crystallographic equivalent nitrogen sites while the carbon atoms move slightly around C0 and C1 positions above the glass transition temperature (around 200 K). This reorientation motions freezes below the transition temperature and lead a random distribution of carbon and nitrogen based on the disordered model for MA^+ below the glass transition. The glass transition in **1-Ti** is distinct from the frozen behavior that commonly observed in similar organic-inorganic hybrid materials.[42,43]

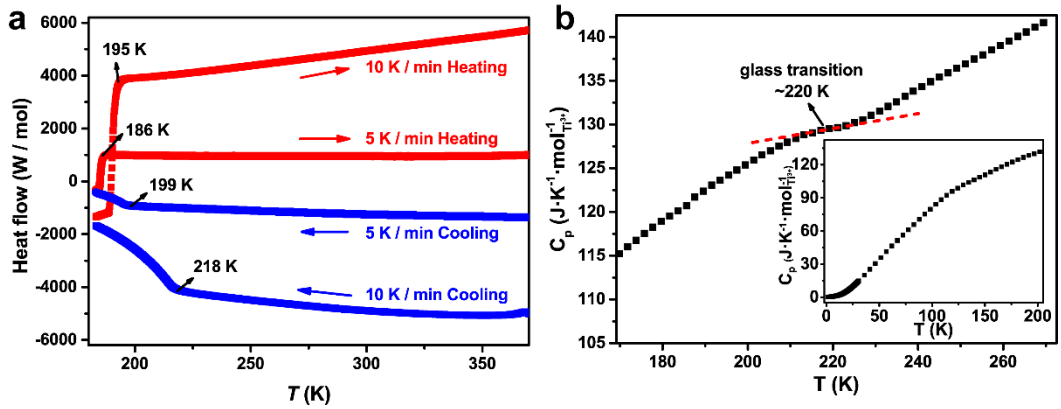

Figure 3. (a) DSC curves for **1-Ti,** blue dots represent the cooling curve, and the red dots represent the heating curve (temperature range from 183 K to 363 K, scanning rate: 5 K / min and 10 K / min). (b) Temperature dependence of heat capacity C_p in **1-Ti** from 160 K to 273 K (high-temperature range). Inset: Temperature dependence of heat capacity C_p in **1-Ti** from 1.8 K to 200 K (low-temperature range).

Physical properties measurement. The magnetic susceptibility measurement of **1-Ti** was performed at several magnetic fields (0.1 to 7.0 T) from 1.8 K to 300 K (Fig. 4). The absence of divergence between field cooling (FC) and zero-field cooling (ZFC) susceptibilities suggests that there is no spin glass state in **1-Ti**. The magnetic susceptibilities of **1-Ti** are field-independent at high-temperature but diverge between 1.8 K to 20 K. In the low-temperature regime, the susceptibility decreases with a higher applied magnetic field. However, no long-range ordering is observed with increasing field. The lack of long-range ordering can be further supported by the specific heat measurement since no sharp peak is observed down to 1.8 K (Inset of Fig. 3b). Fits inverse susceptibility data at high temperature (from 150 K to 300 K) at 0.1 T to the Curie-Weiss law yield a negative Curie-Weiss temperature, θ_{cw} = -139.5(7) K, which indicate the strong antiferromagnetic exchange interactions in **1-Ti** (Fig. 4b). This Curie-Weiss temperature is significantly lower than the previously reported titanium-based KLAFs, $Rb_2NaTi_3F_{12}$, $Cs_2NaTi_3F_{12}$ and $Cs_2KTi_3F_{12}$ (θ_{cw} range from -43 K to -47 K), which share similar connectivity to **1-Ti**, but are significantly distorted from an ideal kagome lattice.[25] A comparison of the structural parameters and the magnetic properties between these Ti^{3+} based KLAFs is listed in Table 1. The effective magnetic moment of μ_{eff} = 1.84 μ_B/Ti^{3+} is close to the theoretical value for spin-1/2 Ti^{3+} ions (1.73 μ_B/Ti^{3+}). The $d\chi^{-1}$ / dT remains constant above 40 K but increase gradually below 40 K (solid blue line in Fig. 4b), which indicates deviation from Curie-Weiss behavior. This deviation suggests the development of short-range antiferromagnetic correlation in **1-Ti,** which is commonly found in highly-frustrated systems.[25,44] Therefore, the absence of long-range ordering down to 1.8 K, the strong antiferromagnetic interaction between spins and the deviation from the Curie-Weiss behavior at low temperature are suggestive for the existence of a QSL state in **1-Ti** at low temperature.

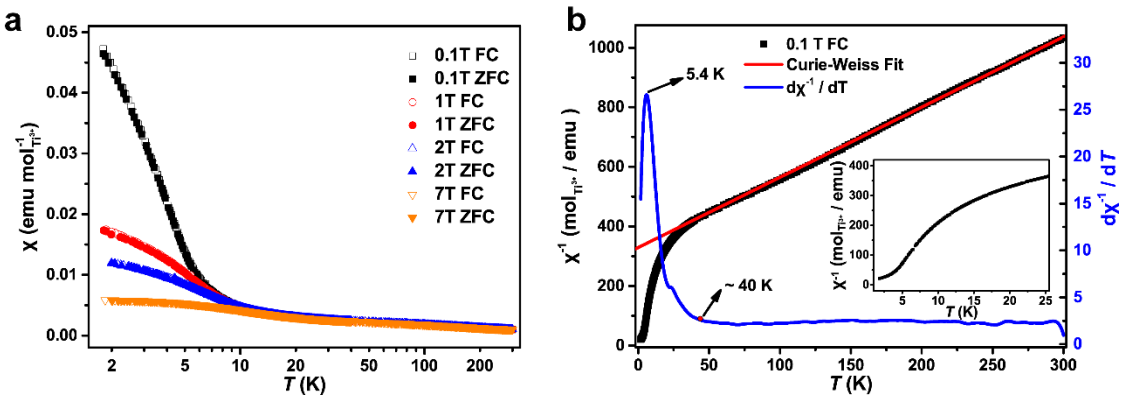

Figure 4. (a) Temperature dependence of magnetic susceptibility in **1-Ti** as measured under ZFC and FC conditions under applied magnetic field. (b) Temperature dependence of inverse magnetic susceptibility in **1-Ti** (left axis, black dots) and the differential susceptibility $d\chi^{-1}$ / dT curves (right axis, blue line) from 1.8 K to 300 K at 0.1 T FC condition. The solid red line is the Curie-Weiss fit from 150 K to 300 K. Inset: Temperature dependence of inverse magnetic susceptibility from 1.8 K to 25 K in **1-T** at 0.1 T FC condition.

The field dependent magnetization up to 14 T at 1.8 K is shown in Fig. 5. The magnetization increases rapidly below 8 T. When the field is higher than 8 T, the magnetization becomes linearly dependent on the field. The magnetization at 14 T is 0.101 μ_B/Ti^{3+} which is far below the value for fully saturated Ti^{3+} ions (1.00 μ_B/Ti^{3+} when g = 2.00). The magnetization can be decomposed into the defect (M_d) and the intrinsic (M_i) contribution and the total magnetization $M = M_d + M_i$. At lower magnetic field (H < 8 T), the $M_i = \chi H$ and the defect magnetization, M_d, approaches saturation. The red dashed line in Fig. 5 is the linear fit for the data with H > 10 T. The intercept of this line with Y-axis is 0.0459 μ_B/Ti^{3+}, and the slope is 0.00397

$\mu_B \cdot T^{-1}/Ti^{3+}$. The defect contribution (orange dots) is obtained by subtracting the linear contribution. The Brillouin function for 4.59% (when g = 2.00) of free S = 1/2 spins (green dashed line) does not match well with the defect contribution which indicates that these defects are not simply the free S = 1/2 paramagnetic spins. The existence of S = 1 impurities cannot be ruled out since the Ti^{2+} could exist in the solid state.[33,45] An inversion point can be observed at 5.4 K (Fig. 4b) and the decrease of slope in the temperature dependence inverse susceptibility is found below 5.4 K with lower temperature (inset of Fig. 4b.) Such a sudden change of slope at low temperature could originate from these magnetic impurities.[44] Nonetheless, the percentage of the impurities in **1-Ti** (~ 4.6% if S = 1/2 and ~2.3% if S = 1 for the magnetic impurities) is smaller than the impurities observed in $ZnCu_3(OH)_6Cl_2$ (range from 5% to 15%) and should not alter the KLAF magnetism in **1-Ti**.[14]

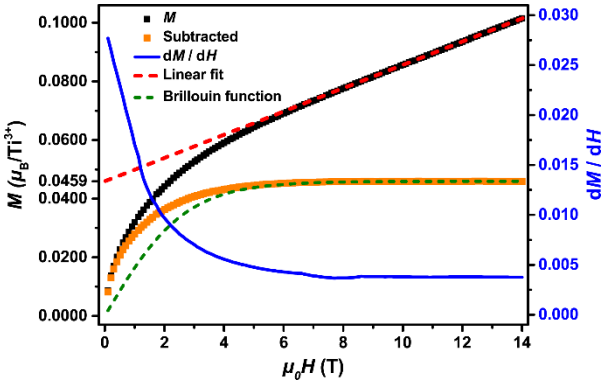

Figure 5. Magnetic field dependence of magnetization (left axis, black dots) and the differential magnetization d*M* / d*H* (right axis, blue line) in **1-Ti** at 1.8 K from 0 to 14 T. The red dashed line is the linear fit magnetization curves from 10 T to 14 T. The orange dots are magnetization data after the subtraction of the linear contribution. The green short dashed line is the Brillouin function for 4.59% of free S = 1/2 spins when g = 2.00.

Table 1. Comparison between the structural information and the magnetic properties of the **1-Ti** and other $A_2BTi_3F_{12}$ compounds

Compounds	Space group	Distances between the neighboring titanium (Å)	Bond angle of ∠Ti-F-Ti (˚)	Curie-Weiss temperature (K)	Effective magnetic moment (μ_B/ Ti^{3+})	Description of the crystal structure	Ref.
1-Ti	$R\bar{3}m$	3.8523(1)	146.09(4)	-139.5(7)	1.84	Perfect kagome lattice with disordered MA^+	this work
$Rb_2NaTi_3F_{12}$	$P2_1/m$	3.799 – 3.844	137.1 – 144.1	-43	1.73	Kagome lattice, largest distortion	23
$Cs_2NaTi_3F_{12}$	$P2_1/m$	3.733 – 3.794	139.2 – 143.5	-44	1.71	Kagome lattice, medium distortion	23
$Cs_2KTi_3F_{12}$	$P2_1/m$	3.831 – 3.849	142.0 – 145.8	-47	1.74	Kagome lattice, smallest distortion	23

Conclusions

In summary, a Ti^{3+} based structurally perfect KLAF, **1-Ti**, was synthesized hydrothermally. A perfect kagome lattice with $R\bar{3}m$ space group and one distinct Ti^{3+} site are observed in **1-Ti**. The trivalent oxidation state and the compressed Jahn-Teller distortion of the trivalent titanium in **1-Ti** are demonstrated by the SCXRD, XPS, and UV-vis-NIR DRS results. This structurally perfect kagome lattice phase is stable from 1.8 K to 523 K based on the low-temperature SCXRD, VT-PXRD, DSC, and specific heat measurements. The DSC measurement also suggests a glass transition around 200 K in **1-Ti** which might originate from the interlayer disordered MA^+. The Curie-Weiss temperature, θ_{cw} = -139.5(7) K, and lack of long-range ordering in magnetic susceptibility and specific heat measurement suggest that the **1-Ti** is a highly frustrated antiferromagnet with QSL behaviors at low-temperature. Importantly for the consideration of emergent magnetic phases, less than 5% of magnetic impurities are observed in **1-Ti** based on the isothermal magnetization measurement at 1.8 K.

Methods

General methods. All reagents were obtained from commercial suppliers without further purification. Deionized water with a resistivity of 18.2 MΩ·cm was used for all synthesis. The hydrothermal reaction was carried out in 23 mL Teflon-lined pressure vessels (Parr 4749), which were purchased from Parr Instruments.

Synthesis of $(CH_3NH_3)_2NaTi_3F_{12}$ (1-Ti). Single crystals of **1-Ti** were synthesized by a conventional hydrothermal method. Ti powder (71.8 mg, 1.5 mmol, 100 mesh), NaF (10.5 mg, 0.25 mmol), CH_3NH_2·HCl (33.8 mg, 0.50 mmol), and deionized water (2.0 mL) were premixed in a 23 mL Teflon liner. An HPF_6 aqueous solution (0.44 mL, 60 w/w%) was added to the mixture in Teflon liner, and the stainless-steel Parr vessel equipped with the Teflon vessel was sealed immediately. The Parr vessel was put in a pre-heated gravity convection lab oven at 363 K for 42 hours under autogenous pressure and then cooled to room temperature at a rate of 0.5 K / minute. Pink prismatic crystals were isolated from the liner by vacuum filtration, washed with deionized water and ethanol sequentially, and dried in air for 2 hours to afford 45.7 mg of **1-Ti** (yield 21% based on titanium, 42% based on sodium). The bulk purity and the stability of **1-Ti** in air are confirmed by PXRD as shown in Fig. S3.

Single crystal X-ray diffraction. Single crystals of **1-Ti** were adhered to Mitegen loops with paratone oil. Data were collected using a XtaLAB Synergy-S diffractometer equipped with a HyPix detector at T = 100.00(10) K or 297.5(3) K. Data were measured using ω scans using Mo Kα radiation. The diffraction pattern was indexed and the total number of runs and images was based on the strategy calculation from the program **CrysAlisPro.**[46] Data reduction, scaling and absorption corrections were performed using **CrysAlisPro.**[46] A numerical absorption correction was performed using **CrysAlisPro.**[46] An empirical absorption correction as implemented in SCALE3 ABSPACK was also applied. The structure was solved and the space group $R\bar{3}m$ (# 166) determined by the ShelXT 2018/3[47-49]. Details of the structural refinement are included in the Supplementary Information.

Powder X-ray diffraction. Powder X-ray diffraction patterns were obtained with a PANalytical X'Pert PRO Alpha-1 diffractometer using 1.8 kW Ceramic copper tube source at room temperature. The simulations of PXRD patterns from SCXRD results are performed by software Crystal Diffract 6. The variable temperature PXRD patterns were collected with an Anton Paar XRK hot stage over the range 300 K ≤ T

≤ 673 K between 2θ = 10 and 90° on PANalytical Empyrean diffractometer. A stream of nitrogen was passed through the hot stage to reduce reactions with ambient air. Each pattern was collected for 10 minutes to obtain signals with a heating rate of 5 K / min.

UV-vis-NIR diffuse reflectance spectra. UV-vis-NIR diffuse reflectance spectra of the **1-Ti** were recorded on a UV-vis-NIR spectrophotometer (UH4150, Hitachi) with an integrating sphere attachment within the range of 200 – 2600 nm and $BaSO_4$ was used as the reflectance standard.

X-ray photoelectron spectroscopy. X-ray photoelectron spectroscopy data were recorded using a Thermo K-Alpha spectrometer with an Al Kα source (hv = 1486.6 eV). The peak fit was conducted in the Thermo Scientific ™ Avantage software. The adventitious C 1s at 284.8 eV was used as a reference for the binding energies as shown in Fig. S8,

Thermal analysis. Thermogravimetric analysis (TGA) measurement was carried out on a Mettler Toledo instruments TGA/DSC 3+ in the temperature range of 298 - 673 K with a ramp rate of 3 K / min. The differential scanning calorimetry (DSC) measurements were carried out using Mettler Toledo instruments TGA/DSC 3+ with the scanning rate of 5 K / min and 10 K / min on cooling/heating in the temperature range of 183 – 363 K. The scans were all performed in flowing nitrogen (flow rate: 80 mL / min).

Physical properties measurement. DC magnetic susceptibility measurements and isothermal magnetization measurements were performed on the **1-Ti** using a Quantum Design physical property measurement system (PPMS) vibrating sample magnetometer in a range of magnetic fields $0 \leq \mu_0 H \leq 14$ T and temperatures $1.8 \leq T \leq 300$ K. The Curie-Weiss temperature θ_{cw} was derived from the linear fitting of data within a certain range with the Curie-Weiss law. The magnetic effective moment, μ_{eff}, was derived from the following equation, $\mu_{eff} = (8C)^{1/2}$. Heat-capacity measurements were carried out on a Quantum Design PPMS. The powder measurements were made on pellets of **1-Ti**. The low-temperature data was measured from 1.8 K to 200 K with Apiezon N grease (The Apiezon N grease cannot be used from 200 K to 240 K due to the existence of the step-like anomaly at around 215 K).[50] The high-temperature data was measured from 160 K to 273 K with Apiezon H grease.

Data availability

The X-ray crystallographic data for **1-Ti** have been deposited at the Cambridge Crystallographic Data Centre (CCDC) under deposition number CCDC 1950701 (**1-Ti**, 100 K) and 1950702 (**1-Ti**, 298 K). These data can be obtained free of charge from The Cambridge Crystallographic Data Centre (www.ccdc.cam.ac.uk/data_request/cif). All the other data supporting the findings of this study are available within the article and its Supplementary Information.

Acknowledgement

Studies were supported by the Beckman Foundation as part of a Beckman Young Investigator Award to H.S.L. Single-crystal diffraction experiments were performed at the Georgia Institute of Technology SCXRD facility directed by Dr. John Bacsa and established with funding from the Georgia Institute of Technology. We thank Prof. Martin Mourigal and Marcus Daum for providing access to a PPMS. This work was performed in part at the Georgia Tech Institute for Electronics and Nanotechnology, a member of the National Nanotechnology Coordinated Infrastructure (NNCI), which is supported by the National Science

Foundation (Grant ECCS-1542174).

Author contributions

N.J. and H.S.L. conceived and designed the experiments. N.J. performed all the experiments except for the TGA, which was performed by A.R. The crystallography was performed by N.J. and J.B. N.J. and H.S.L. wrote the initial draft of the paper and all authors contributed to the final version.

Competing interests

The authors declare no competing interests.

References

1 Ramirez, A. Strongly geometrically frustrated magnets. *Annu. Rev. Mater. Sci.* **24**, 453-480 (1994).

2 Atwood, J. L. Kagome lattice: a molecular toolkit for magnetism. *Nat. Mater.* **1**, 91 (2002).

3 Grohol, D., Nocera, D. G. & Papoutsakis, D. Magnetism of pure iron jarosites. *Phys. Rev. B: Condens. Matter* **67**, 064401 (2003).

4 Obradors, X. *et al.* Magnetic frustration and lattice dimensionality in $SrCr_8Ga_4O_{19}$. *Solid State Commun.* **65**, 189-192 (1988).

5 Freedman, D. E. *et al.* Frustrated magnetism in the S = 1 kagome lattice $BaNi_3(OH)_2(VO_4)_2$. *Chem. Commun.* **48**, 64-66 (2012).

6 Paul, G., Choudhury, A., Sampathkumaran, E. V. & Rao, C. N. R. Organically Templated Mixed‐Valent Iron Sulfates Possessing Kagomé and Other Types of Layered Networks. *Angew. Chem. Int. Ed.* **41**, 4297-4300 (2002).

7 Grohol, D. *et al.* Spin chirality on a two-dimensional frustrated lattice. *Nat. Mater.* **4**, 323 (2005).

8 Hara, S., Sato, H. & Narumi, Y. Exotic magnetism of novel S = 1 kagome lattice antiferromagnet $KV_3Ge_2O_9$. *J. Phys. Soc. Jpn.* **81**, 073707 (2012).

9 Balents, L. Spin liquids in frustrated magnets. *Nature* **464**, 199 (2010).

10 Yan, S., Huse, D. A. & White, S. R. Spin-liquid ground state of the S = 1/2 kagome Heisenberg antiferromagnet. *Science* **332**, 1173-1176 (2011).

11 Shores, M. P., Nytko, E. A., Bartlett, B. M. & Nocera, D. G. A structurally perfect S = 1/2 kagome antiferromagnet. *J. Am. Chem. Soc.* **127**, 13462-13463 (2005).

12 Han, T.-H. *et al.* Fractionalized excitations in the spin-liquid state of a kagome-lattice antiferromagnet. *Nature* **492**, 406 (2012).

13 Freedman, D. E. *et al.* Site specific X-ray anomalous dispersion of the geometrically frustrated kagomé magnet, herbertsmithite, $ZnCu_3(OH)_6Cl_2$. *J. Am. Chem. Soc.* **132**, 16185-16190 (2010).

14 Mendels, P. & Bert, F. Quantum kagome antiferromagnet $ZnCu_3(OH)_6Cl_2$. *J. Phys. Soc. Jpn.* **79**, 011001 (2010).

15 Okamoto, Y., Yoshida, H. & Hiroi, Z. Vesignieite $BaCu_3V_2O_8(OH)_2$ as a candidate spin-1/2 kagome antiferromagnet. *J. Phys. Soc. Jpn.* **78**, 033701-033701 (2009).

16 Yoshida, M., Okamoto, Y., Takigawa, M. & Hiroi, Z. Magnetic order in the spin-1/2 kagome antiferromagnet vesignieite. *J. Phys. Soc. Jpn.* **82**, 013702 (2012).

17 Aidoudi, F. H. *et al.* An ionothermally prepared S = 1/2 vanadium oxyfluoride kagome lattice. *Nat. Chem.* **3**, 801 (2011).

18 Clark, L. *et al.* Gapless spin liquid ground state in the S = 1/2 vanadium oxyfluoride kagome antiferromagnet $[NH_4]_2[C_7H_{14}N][V_7O_6F_{18}]$. *Phys. Rev. Lett.* **110**, 207208 (2013).

19 Nocera, D. G., Bartlett, B. M., Grohol, D., Papoutsakis, D. & Shores, M. P. Spin frustration in 2D kagome lattices: A problem for inorganic synthetic chemistry. *Chem. Eur. J.* **10**, 3850-3859 (2004).

20 Bendix, J., Brorson, M. & Schaffer, C. E. Accurate empirical spin-orbit coupling parameters. zeta. nd for gaseous ndq transition metal ions. The parametrical multiplet term model. *Inorg. Chem.* **32**, 2838-2849 (1993).

21 Jeschke, H. O., Nakano, H. & Sakai, T. From kagome strip to kagome lattice: Realizations of frustrated S = 1/2 antiferromagnets in Ti(III) fluorides. *Phys. Rev. B: Condens. Matter* **99**, 140410 (2019).

22 Sabatier, R. *et al.* Structural and magnetic studies of cesium fluorotitanate ($CsTiF_4$). *Mater. Res. Bull.* **17**, 369-377 (1982).

23 Dadachov, M. & Eriksson, L. Diammonium titanium pentafluoride,$(NH_4)_2TiF_5$, containing Ti^{3+}. *Acta Crystallogr. Sect. C: Cryst. Struct. Commun.* **55**, 1739-1741 (1999).

24 Jo, V., Lee, D. W., Koo, H.-J. & Ok, K. M. $A_2TiF_5 \cdot nH_2O$ (A = K, Rb, or Cs; n = 0 or 1): Synthesis, structure, characterization, and calculations of three new uni-dimensional titanium fluorides. *J. Solid State Chem.* **184**, 741-746 (2011).

25 Goto, M. *et al.* Various disordered ground states and 1/3 magnetization-plateau-like behavior in the S = 1/2 Ti^{3+} kagome lattice antiferromagnets $Rb_2NaTi_3F_{12}$, $Cs_2NaTi_3F_{12}$, and $Cs_2KTi_3F_{12}$. *Phys. Rev. B: Condens. Matter* **94**, 104432 (2016).

26 Armstrong, J. A., Williams, E. R. & Weller, M. T. Fluoride-rich, hydrofluorothermal routes to functional transition metal (Mn, Fe, Co, Cu) fluorophosphates. *J. Am. Chem. Soc.* **133**, 8252-8263 (2011).

27 Jeon, N. J. *et al.* Solvent engineering for high-performance inorganic–organic hybrid perovskite solar cells. *Nat. Mater.* **13**, 897 (2014).

28 Weller, M. T., Weber, O. J., Henry, P. F., Di Pumpo, A. M. & Hansen, T. C. Complete structure and cation orientation in the perovskite photovoltaic methylammonium lead iodide between 100 and 352 K. *Chem. Commun.* **51**, 4180-4183 (2015).

29 Brese, N. & O'keeffe, M. Bond-valence parameters for solids. *Acta Crystallogr. Sect. B: Struct. Sci.* **47**, 192-197 (1991).

30 Brown, I. A determination of the oxidation states and internal stresses in $Ba_2YCu_3O_x$, x= 6–7 using bond valences. *J. Solid State Chem.* **82**, 122-131 (1989).

31 Reinen, D., Atanasov, M., Köhler, P. & Babel, D. Jahn–Teller coupling and the influence of strain in T_g and E_g ground and excited states–A ligand field and DFT study on halide $M^{III}X_6$ model complexes [M= Ti^{III}–Cu^{III}; X= F^-, Cl^-]. *Coord. Chem. Rev.* **254**, 2703-2754 (2010).

32 Rao, C. N. R. *et al.* Synthesis, structure, and the unusual magnetic properties of an amine-templated iron (II) sulfate possessing the Kagome lattice. *Chem. Mater.* **16**, 1441-1446 (2004).

33 Koelle, U. & Koelle, P. Aqueous chemistry of titanium (II) species. *Angew. Chem. Int. Ed.* **42**, 4540-4542 (2003).

34 Mousty-Desbuquoit, C., Riga, J. & Verbist, J. J. Electronic structure of titanium (III) and titanium (IV) halides studied by solid-phase X-ray photoelectron spectroscopy. *Inorg. Chem.* **26**, 1212-1217 (1987).

35 Nyholm, R., Martensson, N., Lebugle, A. & Axelsson, U. Auger and Coster-Kronig broadening effects in the 2p and 3p photoelectron spectra from the metals ^{22}Ti-^{30}Zn. *J. Phys, F: Met. Phys.* **11**, 1727 (1981).

36 Hüfner, S. *Photoelectron spectroscopy: principles and applications*. (Springer Science & Business Media, 2013).

37 Kesari, Y. & Athawale, A. Ultrasound assisted bulk synthesis of $CH_3NH_3PbI_3$ perovskite at room temperature. *Mater. Lett.* **159**, 87-89 (2015).

38 Reisinger, S. A., Tang, C. C., Thompson, S. P., Morrison, F. D. & Lightfoot, P. Structural Phase Transition in the S = 1/2 Kagome System $Cs_2ZrCu_3F_{12}$ and a Comparison to the Valence-Bond-Solid Phase in $Rb_2SnCu_3F_{12}$. *Chem. Mater.* **23**, 4234-4240 (2011).

39 Ono, T. *et al.* Magnetic susceptibilities in a family of S = 1/2 kagome antiferromagnets. *Phys. Rev. B: Condens. Matter* **79**, 174407 (2009).

40 Kelly, Z. A., Tran, T. T. & McQueen, T. M. Nonpolar-to-Polar Trimerization Transitions in the S = 1 Kagome Magnet $Na_2Ti_3Cl_8$. *Inorg. Chem.* (2019).

41 Donth, E. *The glass transition: relaxation dynamics in liquids and disordered materials*. Vol. 48 (Springer Science & Business Media, 2013).

42 Guo, Y. *et al.* Interplay between organic cations and inorganic framework and incommensurability in hybrid lead-halide perovskite $CH_3NH_3PbBr_3$. *Phys. Rev. Mater.* **1**, 042401 (2017).

43 Fabini, D. H. *et al.* Universal dynamics of molecular reorientation in hybrid lead iodide perovskites. *J. Am. Chem. Soc.* **139**, 16875-16884 (2017).

44 Bert, F. *et al.* Low temperature magnetization of the S = 1/2 kagome antiferromagnet $ZnCu_3(OH)_6Cl_2$. *Phys. Rev. B: Condens. Matter* **76**, 132411 (2007).

45 Bartkowski, S. *et al.* Electronic structure of titanium monoxide. *Phys. Rev. B: Condens. Matter* **56**, 10656 (1997).

46 CrysAlisPro Software system v. 1.171.39.20a (Rigaku Corporation, 2015).

47 Sheldrick, G. M. Crystal structure refinement with SHELXL. *Acta Crystallogr. C* **71**, 3-8 (2015).

48 Sheldrick, G. M. SHELXT–Integrated space-group and crystal-structure determination. *Acta Crystallorgr., Sect. A: Found. Adv.* **71**, 3-8 (2015).

49 Dolomanov, O. V., Bourhis, L. J., Gildea, R. J., Howard, J. A. & Puschmann, H. OLEX2: a complete structure solution, refinement and analysis program. *J. Appl. Crystallogr.* **42**, 339-341 (2009).

50 Schnelle, W., Engelhardt, J. & Gmelin, E. Specific heat capacity of Apiezon N high vacuum grease and of Duran borosilicate glass. *Cryogenics* **39**, 271-275 (1999).

Synthesis of a Structurally Perfect d^1 Kagome Lattice Antiferromagnet, $(CH_3NH_3)_2NaTi_3F_{12}$

Ningxin Jiang[1], Arun Ramanathan[1], John Bacsa[1], and Henry S. La Pierre[1,2]*

[1]School of Chemistry and Biochemistry and the [2]Nuclear and Radiological Engineering Program, School of Mechanical Engineering, Georgia Institute of Technology, Atlanta, Georgia 30332-0400, United States.
*e-mail: hsl@gatech.edu

Table of contents

1. Further synthetic details

Synthesis of $KTiF_4$. Single crystals of $KTiF_4$ were synthesized by a hydrothermal method. Ti powder (71.8 mg, 1.5 mmol, 100 mesh), KF (58.1 mg, 1.0 mmol) and deionized water (2.0 mL) were premixed in a 23 mL Teflon liner. An aqueous solution of HPF_6 (0.44 mL, 60 w/w%) was added to the mixture in the Teflon liner, and the stainless-steel Parr vessel equipped with the Teflon vessel was sealed immediately. The Parr vessel was put in a pre-heated, gravity convection oven at 393 K for 18 hours under autogenous pressure and then cooled to room temperature at a rate of 0.5 K / minute. Pink prismatic crystals were isolated from the liner by vacuum filtration, washed with deionized water and ethanol sequentially, and dried in air for 2 hours to afford 96.3 mg of $KTiF_4$ (yield 39% based on titanium). Bulk purity of the as-synthesized $KTiF_4$ was confirmed by comparing the experimental powder X-ray diffraction (PXRD) pattern with the simulated PXRD pattern based on the previously reported crystallographic data (Fig. S5).[1]

Synthesis of Na_3TiF_6. A powder sample of Na_3TiF_6 was synthesized by a hydrothermal method. Ti powder (95.7 mg, 2 mmol, 100 mesh), $Na_2(PO_3F)$ (1439.5 mg, 10 mmol) and deionized water (4 mL) were premixed in a 23 mL Teflon liner. An aqueous solution of HPF_6 (0.29 mL, 60 w/w%) was added to the mixture in the Teflon liner, and the stainless-steel Parr vessel was sealed immediately. The Parr vessel was put in a pre-heated gravity convection oven at 393 K for 18 hours under autogenous pressure and then cooled to room temperature at a rate of 0.5 K / minute. A purple powder was isolated from the liner by vacuum filtrated, washed with deionized water and ethanol sequentially, and dried under a vacuum using Schlenk techniques for 30 minutes to afford 100.8 mg of Na_3TiF_6 (yield 22% based on titanium). Bulk purity of the as-synthesized Na_3TiF_6 was confirmed by comparing the experimental PXRD pattern with the PXRD pattern from the ICDD database (JCPDS card number 26-1491, Na_3TiF_6) (Fig. S6).

2. Crystallographic data and analysis

Data collection and structural refinement details.

Refinement of 1-Ti at 298 K. A pink prism-shaped crystal with dimensions 0.09 × 0.06 × 0.04 mm^3 was mounted on a loop with paratone oil. Data were collected using a XtaLAB Synergy-S diffractometer equipped with a HyPix detector at T = 297.5(3) K. Data were measured using ω scans using Mo Kα radiation. The diffraction pattern was indexed and the total number of runs and images was based on the strategy calculation from the program **CrysAlisPro**.[2] The maximum resolution that was achieved was θ = 37.971° (0.58 Å). The unit cell was refined using **CrysAlisPro** on 3764 reflections, 66% of the observed reflections.[2]

Data reduction, scaling and absorption corrections were performed using **CrysAlisPro**.[2] The final completeness is 100.00 % out to 37.971° in θ. A numerical absorption correction based on Gaussian integration over a multifaceted crystal model was performed using **CrysAlisPro**.[2] An empirical absorption correction using spherical harmonics as implemented in SCALE3 ABSPACK was also applied. The absorption coefficient μ of this material is 1.963 mm^{-1} at this wavelength (λ = 0.711Å) and the minimum and maximum transmissions are 0.906 and 0.949.

The structure was solved and the space group $R\bar{3}m$ (# 166) determined by the ShelXT 2018/3 structure solution program using dual methods and refined by full matrix least squares minimization on F^2 using version 2018/3 of ShelXL 2018/3.[3-5] All non-hydrogen atoms were refined anisotropically. Hydrogen atom positions were calculated geometrically and refined using the riding model.

Refinement of 1-Ti at 100 K. A pink prism-shaped crystal with dimensions 0.12 × 0.09 × 0.08 mm^3 was mounted on a loop with paratone oil. Data were collected using a XtaLAB Synergy-S diffractometer equipped with a HyPix detector and an Oxford Cryosystems low-temperature device operating at T = 100.00(10) K.

Data were measured using ω scans using Mo Kα radiation. The diffraction pattern was indexed and the total number of runs and images was based on the strategy calculation from the program **CrysAlisPro**.[2] The maximum resolution that was achieved was θ = 40.234° (0.55 Å). The unit cell was refined using **CrysAlisPro** on 6854 reflections.[2]

Data reduction, scaling and absorption corrections were performed using **CrysAlisPro**.[2] The final completeness is 93.90 % out to 40.234° in θ. A numerical absorption correction based on Gaussian integration over a multifaceted crystal model was performed using **CrysAlisPro**.[2] An empirical absorption correction using spherical harmonics as implemented in SCALE3 ABSPACK was also used. The absorption coefficient μ of this material is 1.972 mm^{-1} at this wavelength (λ = 0.711Å) and the minimum and maximum transmissions are 0.904 and 0.997.

The structure was solved and the space group $R\bar{3}m$ (# 166) determined by the ShelXT 2018/3 structure solution program using dual methods and refined by full matrix least squares minimization on F^2 using version 2018/3 of ShelXL 2018/3.[3-5] All

non-hydrogen atoms were refined anisotropically. Hydrogen atom positions were located from the electron densities and refined freely.

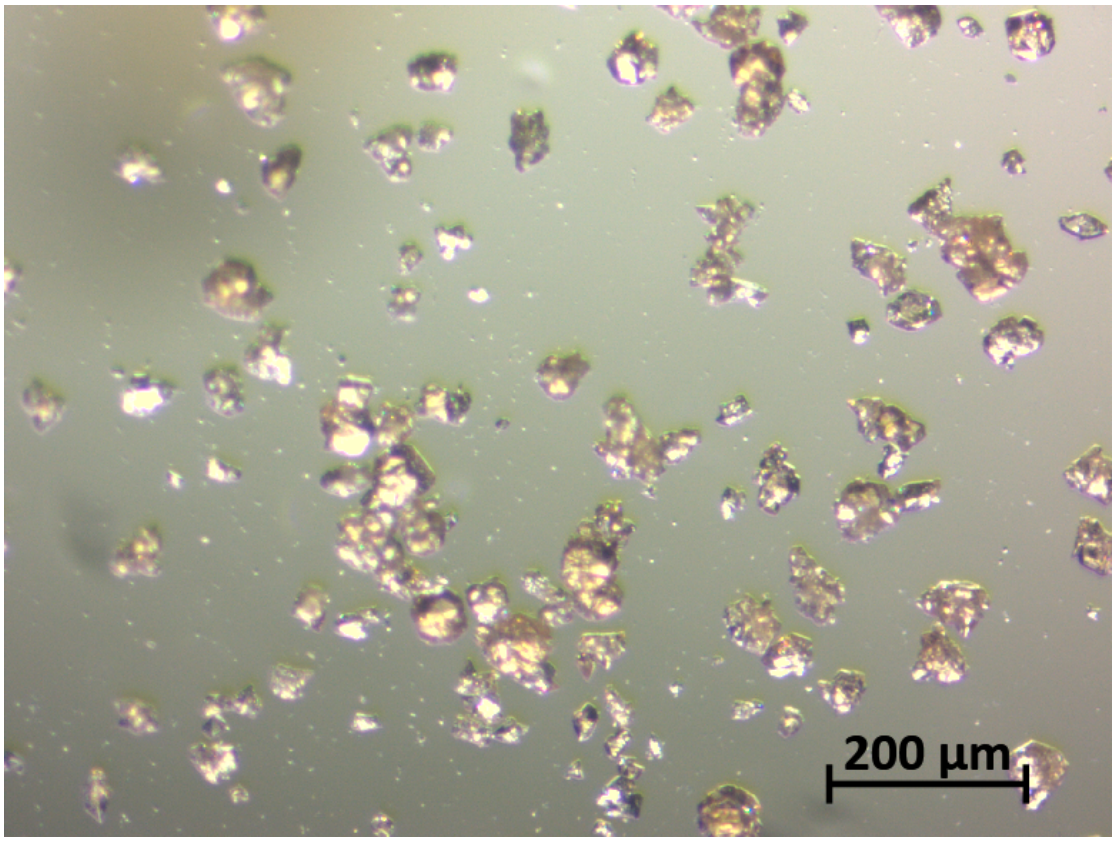

Figure S1. Crystals of **1-Ti**

Table S1. Crystal data and structure refinement for **1-Ti** at 298 K and 100 K

Compound	**1-Ti**	**1-Ti-100 K**
Empirical formula	$(CH_3NH_3)_2NaTi_3F_{12}$	$(CH_3NH_3)_2NaTi_3F_{12}$
$D_{calc.}$/ g cm^{-3}	2.314	2.324
m / mm^{-1}	1.963	1.972
Formula Weight	452.78	452.78
Colour	Pink	Pink
Shape	Prism	Prism
Size / mm^3	0.09 × 0.06 × 0.04	0.12 × 0.09 × 0.08
T / K	297.5(3)	100.00(10)
Crystal System	Trigonal	Trigonal
Space Group	$R\bar{3}$m	$R\bar{3}$m
a / Å	7.7046(2)	7.70241(13)
b / Å	7.7046(2)	7.70241(13)
c / Å	18.9645(6)	18.8899(3)
α / °	90	90
β / °	90	90
γ / °	120	120
V / Å^3	974.94(7)	970.54(4)
Z	3	3
Z'	0.0833	0.0833
F(000)	651.0	651.0
Radiation	MoKα (λ = 0.71073)	MoKα (λ = 0.71073)
2θ range for data collection(°)	6.446 to 75.942	6.47 to 80.468
Index Ranges	-10 ≤ h ≤ 13, -13 ≤ k ≤ 13, -31 ≤ l ≤ 32	-14 ≤ h ≤ 14, -14 ≤ k ≤ 12, -34 ≤ l ≤ 28
Reflections Collected	5694	5810
Independent Reflections	673	772
Data/Restraints/Parameters	673/17/33	772/17/34
Goodness-of-Fit on F^2	1.140	1.089
Final R Indexes [I>=2σ (I)]	R_1 = 0.0220, wR_2 = 0.0606	R_1 = 0.0254, wR_2 = 0.0637
Final R Indexes [all data]	R_1 = 0.0236, wR_2 = 0.0611	R_1 = 0.0257, wR_2 = 0.0638
Largest Diff. Peak/Hole (e / Å^3)	0.67/-0.75	1.74/-1.36
Completeness to 2θ	100%	93.9%

Table S2. Atomic coordinates of **1-Ti** at 298 K and 100 K (Hydrogen atoms are omitted for simplicity)

Atoms	*x / a*	*y / b*	*z / c*	U_{eq}
298 K				
Ti1	5/6	2/3	2/3	0.01039(8)
Na1	1	1	1/2	0.0169(3)
F1	0.85694(8)	0.71387(16)	0.56840(5)	0.0254(2)
F2	0.54364(7)	0.45636(7)	0.65330(5)	0.02278(19)
C0	2/3	1/3	0.4352(5)	0.0449(15)
C1	0.711(2)	0.358(3)	0.4506(7)	0.0449(15)
N1	0.5789(4)	0.4211(4)	0.4774(2)	0.0315(9)
100 K				
Ti1	5/6	2/3	2/3	0.00462(8)
Na1	1	1	1/2	0.0069(2)
F1	0.85781(7)	0.71562(14)	0.56784(4)	0.01211(15)
F2	0.54338(7)	0.45662(7)	0.65277(5)	0.01111(15)
C0	2/3	1/3	0.4391(4)	0.0212(10)
C1	0.7075(16)	0.362(2)	0.4494(6)	0.0212(10)
N1	0.5771(3)	0.4229(3)	0.47797(17)	0.0131(5)

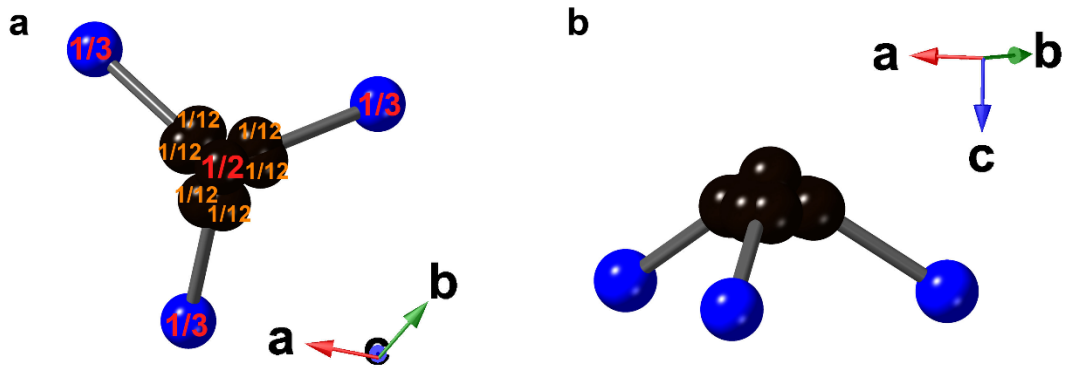

Figure S2. The demonstration of the disorder model for $CH_3NH_3^+$ with the occupancy of carbon or nitrogen sites in the center of the atoms view parallel to the crystallography *c*-axis (left) and viewed perpendicular to the *c*-axis (right). Carbon atoms are black, nitrogen atoms are dark blue, hydrogen atoms are omitted for clarity.

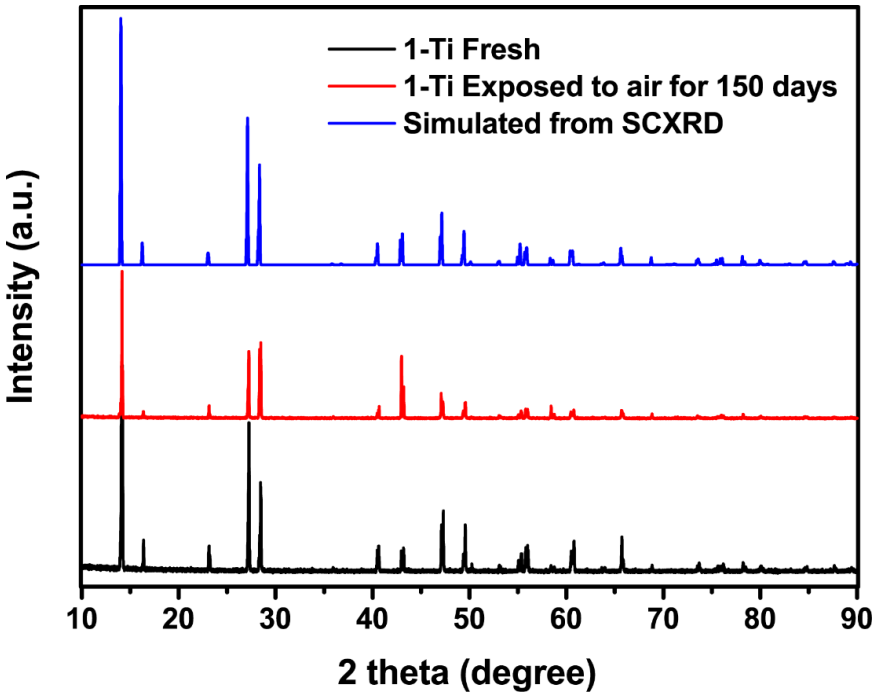

Figure S3. Experimental data of fresh sample (black line), sample exposed to air for 150 days (red line) and the simulated (blue line, simulated from 298 K single-crystal X-ray result) PXRD patterns for **1-Ti**.

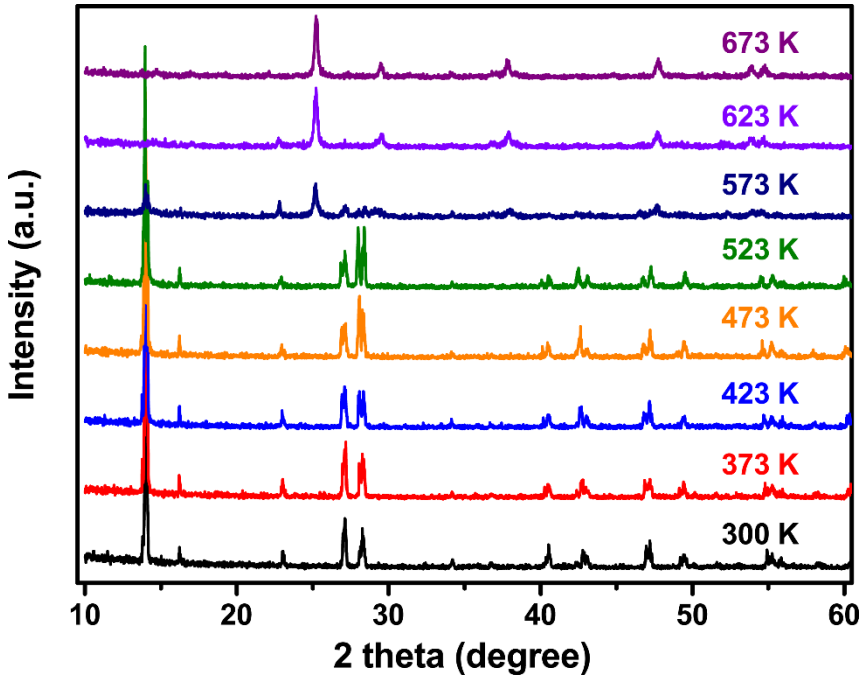

Figure S4. Variable temperature PXRD patterns of **1-Ti** from 300 K to 673 K.

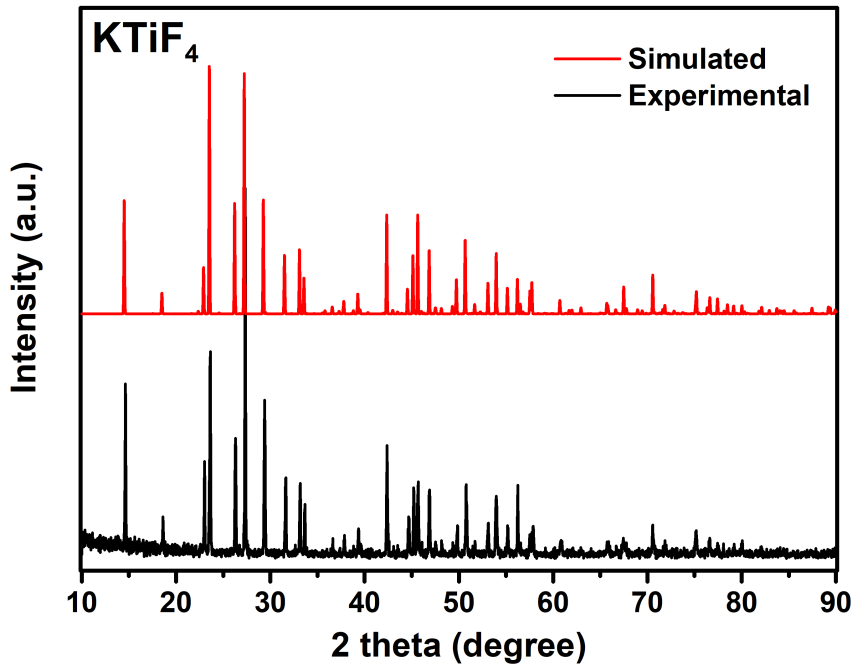

Figure S5. Experimental PXRD patterns (black line) and the simulated (red line, simulated from previously reported single-crystal X-ray diffraction result[1]) PXRD patterns for $KTiF_4$

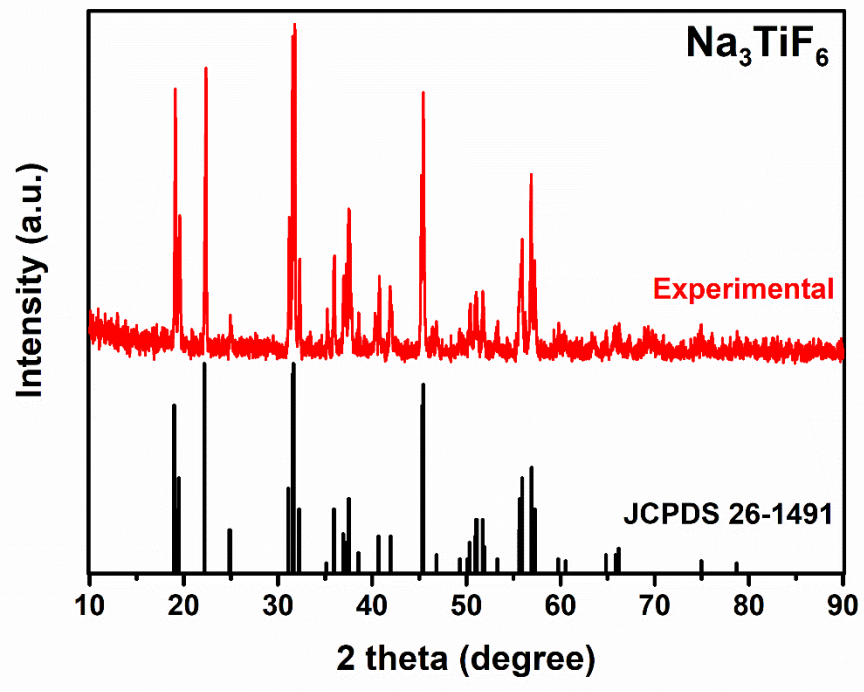

Figure S6. Experimental PXRD patterns (red line) for Na_3TiF_6. Black line: JCPDS no. 26-1491 (Na_3TiF_6).

3. Fourier-transformation infrared spectroscopy (FT-IR)

Infrared (IR) samples were acquired as powder on a Bruker ALPHA FT-IR spectrometer from 400 to 4000 cm^{-1}. The sample was dried under vacuum using Schlenk techniques for an hour prior to the FT-IR measurement. Sample measured under ambient conditions.

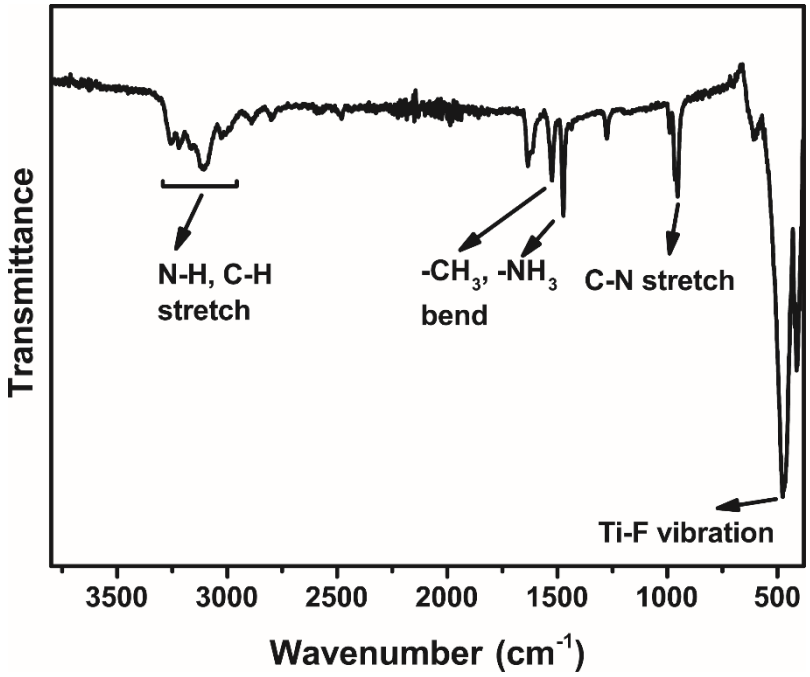

Figure S7. FT-IR spectrum for **1-Ti**.

The assignment of peaks in Fig. S7 is based on literature values.[6,7]

4. X-ray photoelectron spectroscopy (XPS)

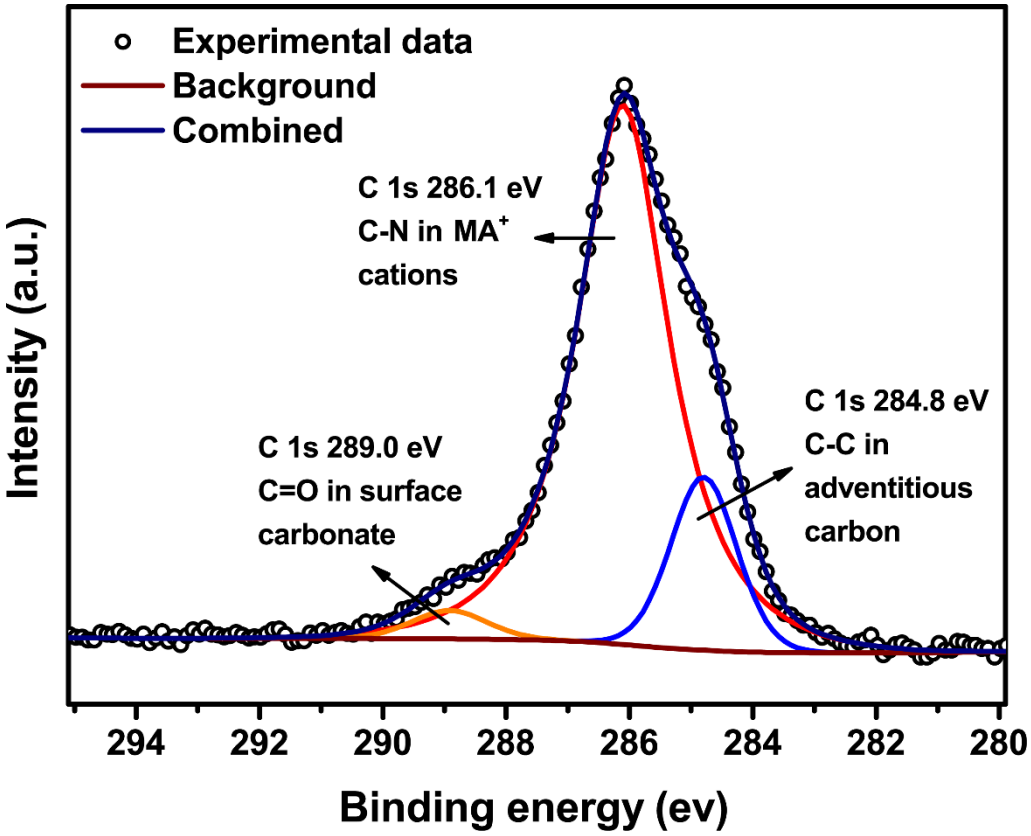

Figure S8. High resolution XPS C 1s spectra of **1-Ti**.

The high-resolution XPS C 1s spectrum of **1-Ti** is shown in Fig. S8. The spectrum is resolved into three peaks. The peak centers at 284.8 eV can be assigned as adventitious carbon and is used as a reference for the binding energies. The peak centers at 286.1 eV can be assigned as the C-N bond in the MA^+.[8] The small peak centers at 289.0 eV is assigned as the surface carbonate since sample is exposed to CO_2 in air.[9]

5. UV-vis-NIR diffuse reflectance spectra (UV-vis-NIR DRS)

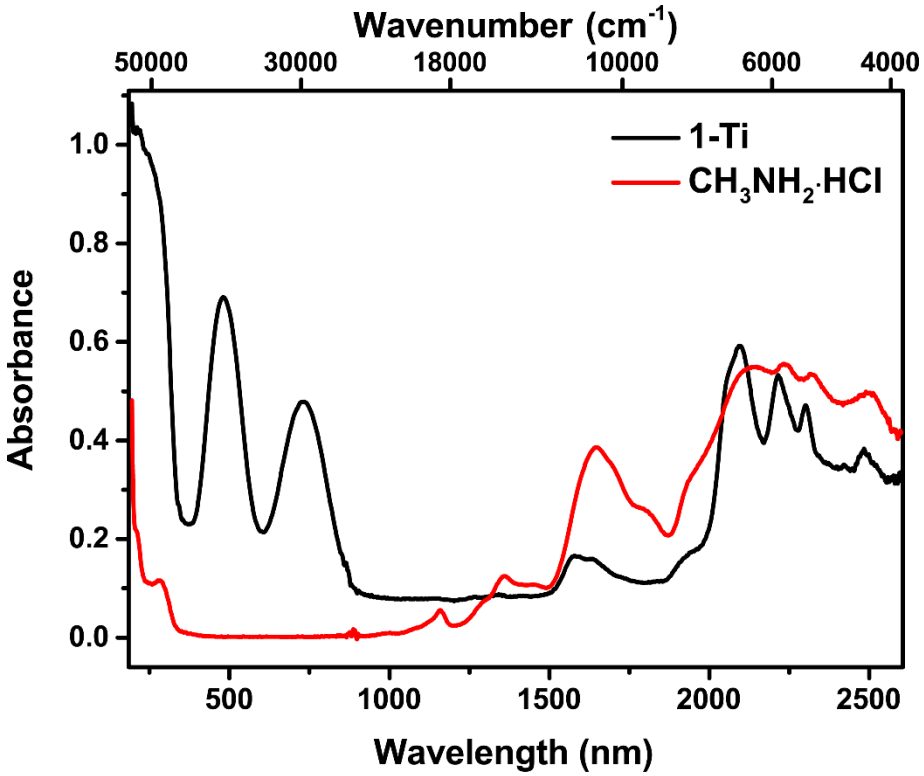

Figure S9. UV-vis-NIR diffuse reflectance spectra of **1-Ti** and CH_3NH_2·HCl at room temperature.

6. Thermogravimetric analysis (TGA)

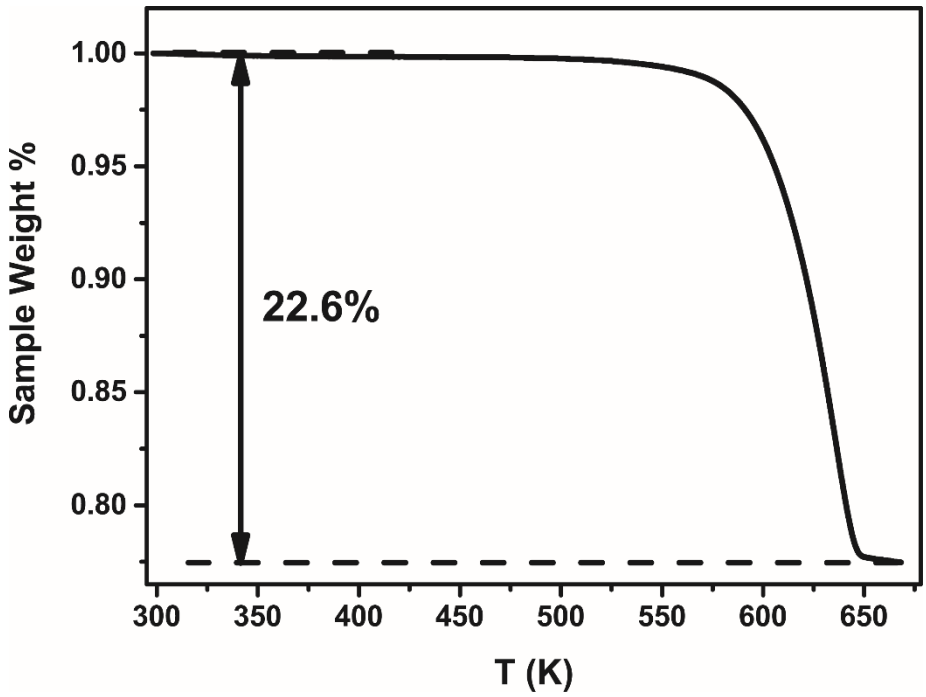

Figure S10. TG profile for **1-Ti** from 298 K to 673 K with ramp rate of 3 K / min.

In Fig. S10, the sample weight remains constant from 298 K to around 523 K, starts to decrease above 523 K and remains stable at around 648 K. The 22.6% weight loss at 648 K can be attributed to the loss of two CH_3NH_2 and two HF for **1-Ti** (theoretical 22.3% for two CH_3NH_2 and two HF in $MA_2NaTi_3F_{12}$) and leaving a material of nominal composition "$NaTiF_4$".

7. References

1 Sabatier, R., Charroin, G., Avignant, D., Cousseins, J. & Chevalier, R. La structure cristalline du fluorotitanate de potassium $KTiF_4$. *Acta Crystallogr. Sect. B Struct. Cryst. Cryst. Chem.* **35**, 1333-1336 (1979).

2 Rigaku Oxford Diffraction, (2015), CrysAlisPro Software system, version 1.171.39.20a, Rigaku Corporation, Oxford, UK.

3 Sheldrick, G. M. Crystal structure refinement with SHELXL. *Acta Crystallogr. Sect. C: Cryst. Struct. Commun.* **71**, 3-8 (2015).

4 Sheldrick, G. M. SHELXT–Integrated space-group and crystal-structure determination. *Acta Crystallorgr., Sect. A: Found. Adv.* **71**, 3-8 (2015).

5 Dolomanov, O. V., Bourhis, L. J., Gildea, R. J., Howard, J. A. & Puschmann, H. OLEX2: a complete structure solution, refinement and analysis program. *J. Appl. Crystallogr.* **42**, 339-341 (2009).

6 Cabana, A. & Sandorfy, C. The infrared spectra of solid methylammonium halides. *Spectrochim. Acta A* **18**, 843-861 (1962).

7 Jo, V., Lee, D. W., Koo, H.-J. & Ok, K. M. $A_2TiF_5 \cdot nH_2O$ (A = K, Rb, or Cs; n = 0 or

1): Synthesis, structure, characterization, and calculations of three new uni-dimensional titanium fluorides. *J. Solid State. Chem.* **184**, 741-746 (2011).

8 Jiang, Y. *et al.* Post-annealing of $MAPbI_3$ perovskite films with methylamine for efficient perovskite solar cells. *Mater. Horiz.* **3**, 548-555 (2016).

9 Shchukarev, A. & Korolkov, D. XPS study of group IA carbonates. *Open Chem.* **2**, 347-362 (2004).